An Untethered, Electrostatic, Globally Controllable MEMS Micro-Robot

Bruce R. Donald, *Member, IEEE*, Christopher G. Levey, *Member, IEEE*, Craig D. McGray, *Member, IEEE*, Igor Paprotny, and Daniela Rus

***Abstract*—We present an untethered, electrostatic, MEMS micro-robot, with dimensions of 60 μm by 250 μm by 10 μm. The device consists of a curved, cantilevered steering arm, mounted on an untethered scratch drive actuator (USDA). These two components are fabricated monolithically from the same sheet of conductive polysilicon, and receive a common power and control signal through a capacitive coupling with an underlying electrical grid. All locations on the grid receive the same power and control signal, so that the devices can be operated without knowledge of their position on the substrate. Individual control of the component actuators provides two distinct motion gaits (forward motion and turning), which together allow full coverage of a planar workspace. These MEMS micro-robots demonstrate turning error of less than 3.7°/mm during forward motion, turn with radii as small as 176 μm, and achieve speeds of over 200 μm/sec with an average step size as small as 12 nm. They have been shown to operate open-loop for distances exceeding 35 cm without failure, and can be controlled through teleoperation to navigate complex paths. The devices were fabricated through a multiuser surface micromachining process, and were postprocessed to add a patterned layer of tensile chromium, which curls the steering arms upward. After sacrificial release, the devices were transferred with a vacuum microprobe to the electrical grid for testing. This grid consists of a silicon substrate coated with 13-μm microfabricated electrodes, arranged in an interdigitated fashion with 2-μm spaces. The electrodes are insulated by a layer of electron-beam-evaporated zirconium dioxide, so that devices placed on top of the electrodes will experience an electrostatic force in response to an applied voltage. Control waveforms are broadcast to the device through the capacitive power coupling, and are decoded by the electromechanical response of the device body. Hysteresis in the system allows on-board storage of $n = 2$ bits of state information in response to these electrical signals. The presence of on-board state information within the device itself allows each of the two device subsystems (USDA and steering arm) to be individually addressed and controlled. We describe this communication and control strategy and show necessary and sufficient conditions for voltage-selective actuation of all 2^n system states, both for our devices ($n = 2$), and for the more general case (where n is larger.) [1586]**

Manuscript received April 26, 2005; revised August 8, 2005. This work was supported by Award 2000-DT-CX-K001 to B. R. Donald from the Office for Domestic Preparedness, Department of Homeland Security, USA. Subject Editor G. Stemme.

B. R. Donald is with the Computer Science Department and the Chemistry Department, Dartmouth College, Hanover, NH 03755 USA (e-mail: brd@cs.dartmouth.edu).

C. G. Levey is with the Thayer School of Engineering, Dartmouth College, Hanover, NH 03755 USA.

C. D. McGray and I. Paprotny are with the Computer Science Department, Dartmouth College, Hanover, NH 03755 USA.

D. Rus is with the the Electrical Engineering and Computer Science Department, Massachusetts Institute of Technology (MIT), Cambrdge, MA 02139 USA.

Digital Object Identifier 10.1109/JMEMS.2005.863697

***Index Terms*—Actuator, control, electrostatic, fabrication, locomotion, MEMS, micro-robot, PolyMUMPS, robotics, scrath-drive, steering, untethered.**

I. Introduction

THIS paper describes the design, fabrication, and control of an untethered, electrostatic, MEMS micro-robot, with bounding dimensions of 60 μm by 250 μm by 10 μm. Fig. 1 shows the structure of this device. It consists of an untethered scratch drive actuator [1] (**A**), with a cantilevered steering arm (**B**) that protrudes from one side. The untethered scratch drive is used for locomotion, while the steering arm is used to raise or lower a stylus into contact with the substrate. When this stylus is in contact with the substrate, it provides enough friction to cause the device as a whole to turn. This provides the device with two distinct motion capabilities: it can either translate forward, or turn through an arc with a fixed minimum radius of approximately 175 μm. Alternation of these two motion primitives allows for execution of turns with any arbitrary radius larger than the minimum.

While there are many MEMS devices with sizes measured in tens of microns, the smallest previously existing micro-robotic systems have dimensions on the order of millimeters or centimeters. A primary reason for this, is that previously existing micro-robot architectures rely on the presence of a rigid chassis on which to mount power, locomotion, steering, communication, and control systems. While these active components often include thin-film MEMS actuators, the chassis is a macroscale part such as, for example, a silicon die. For this reason, these micro-robots are often referred to as "walking chips" [2]–[9].

In a typical walking chip, the mass of the active components may compose only a few tenths of one percent of the total mass of the system. By integrating the locomotion, steering, communication, and control subsystems into a single connected device, we have been able to produce a micro-robot that is one to two orders of magnitude smaller in length than previous systems, and many thousands of times smaller in overall mass.

Previous micro-robotic systems utilized a variety of approaches to solving the problems of power delivery, steering, and control [2], [3], [5]–[7], [9]–[11]. Past systems have delivered power through vibration [12], through photothermal transduction [2], [3], through inductive coupling [4], and electrically through gold bonding wire [6], [7], [9]. The capacitively coupled electrostatic power delivery mechanism that we described in [1] is well-suited to the untethered devices presented in the current paper. Our devices use the power delivery mechanism in [1], and extend it to incorporate high-κ dielectrics.

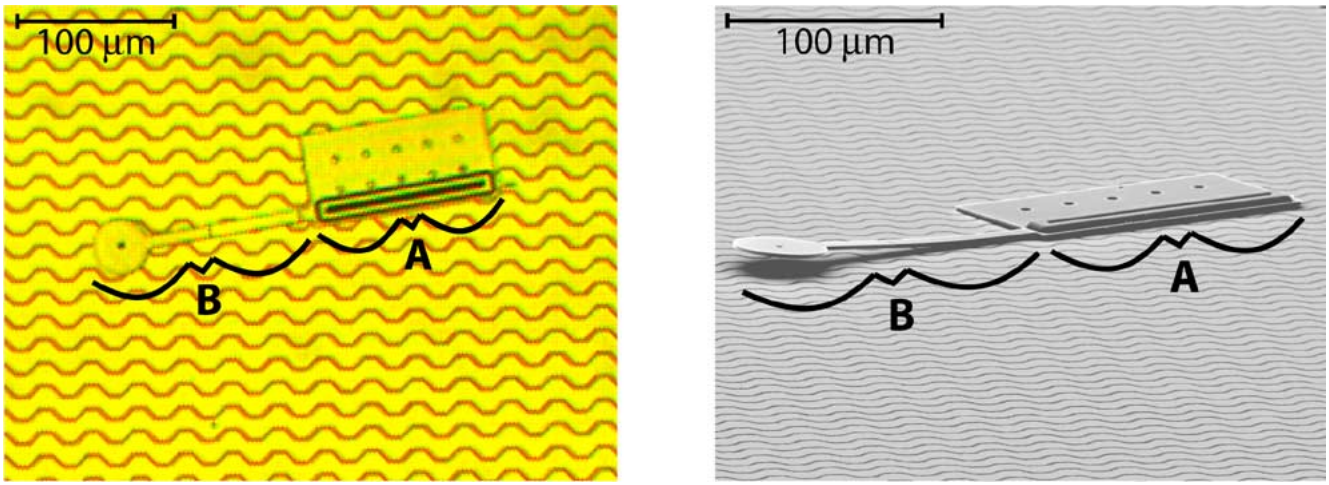

Fig. 1. Optical (left) and electron (right) micrographs of an electrostatic micro-robot. The device consists of an untethered scratch drive actuator (A) [1], with a cantilevered steering arm (B) that protrudes from one side. The untethered scratch drive is used for propulsion, while the steering arm can be raised or lowered to turn. An array of insulated interdigitated electrodes (lighter-colored background) provides electrical power and control signals to the device.

With this mechanism, the device receives its electrical power and control signals through an array of insulated interdigitated electrodes that cover the device's operating environment. Since the control signal and electrical power are both available to the device anywhere within this environment, the device can move freely, untethered by the wires and rails that power most electrostatic MEMS devices. The operating environment used for the devices presented in this paper extends across 6.25 square millimeters of surface, and could easily be made even larger if desired.

In previous micro-robotic devices, steering systems have been implemented primarily through differential operation of matched pairs or arrays of identical actuators [2], [5], [7], [9], [12]. The device described in the present paper uses only two actuators: one for propulsion, and a second one to raise and lower a stylus into frictional contact with the substrate. This simplifies the overall device, reduces its size, and allows for precisely controlled turning motions, even in the presence of small surface abnormalities.

Since the scratch drive and the steering arm are fabricated monolithically from the same sheet of conductive polysilicon, they must have the same voltage at any given time. However, to control the micro-robot, we must be able to independently actuate these two components. To do this, we exploit the electromechanical hysteresis of the components by applying sequences of voltages in a control waveform. When a voltage is applied to the device, it pulls the device's components toward the substrate. Since this electrostatic attraction scales inversely with the distance of separation, these changes in shape have discrete transitions, akin to the snap-down voltages of MEMS relays [13]–[15]. The scratch drive can be either flexed or relaxed, and the steering arm can either be in contact with the substrate, or out of contact. Hence, the state of the device can be discretized into four possible values, according to whether or not each of the two components has crossed its transition point. The control system for the micro-robot can then be treated as a finite state machine, as shown in Fig. 2, and a sequence of voltages can be calculated to transition between any pair of states. To produce a desired behavior (forward motion or turning), a control command is specified by an electrical pulse, and is stored in the elastic flexure of the device subsystems. Then, a continuous ac drive waveform is applied to actuate the scratch drive and produce motion.

This *state-based* approach to micro-robot control contrasts markedly with previous approaches. In the past, the most common approach to controlling micro-robots has been to concurrently and selectively address those subsystems that are required for a particular behavior. This was achieved in most cases by electrically insulating the subsystems from one another, and then directly connecting control signals and electrical power to each subsystem with a thin gold bonding wire [5], [7], [9]. Miura, *et al.* used resonant frequencies of vibration for component addressing [12], while Baglio *et al.* used selective transmittance windows made from photonic band gap materials [2].

The silicon components of the micro-robots presented in this paper are fabricated through the PolyMUMPS process [16]. However, the device design requires components whose z-axis geometries are not attainable using standard thin-film micromachining processes, such as those available through the PolyMUMPS service. Hence, these geometries are achieved in postprocessing using stress-engineering techniques [17], [18]. Section II discusses the device fabrication in detail.

The performance of the devices was tested under both open-loop and teleoperated control. In both cases, an array of insulated interdigitated electrodes on a silicon substrate serves as the operating environment. Microprobes connect these electrodes to a function generator and amplifier. During teleoperation, a human operator switches between two different waveforms produced by the function generator in order to control the motion of the untethered micro-robotic device. A camera records the device's motion through an optical microscope, allowing the operator to make the necessary adjustments to guide the device along the desired path. Section VI discusses the reliability of the basic motion primitives, and shows some examples of complex paths traversed during teleoperation.

Fig. 3 shows the progression of the technology toward the device presented in this paper. This paper enables controllable

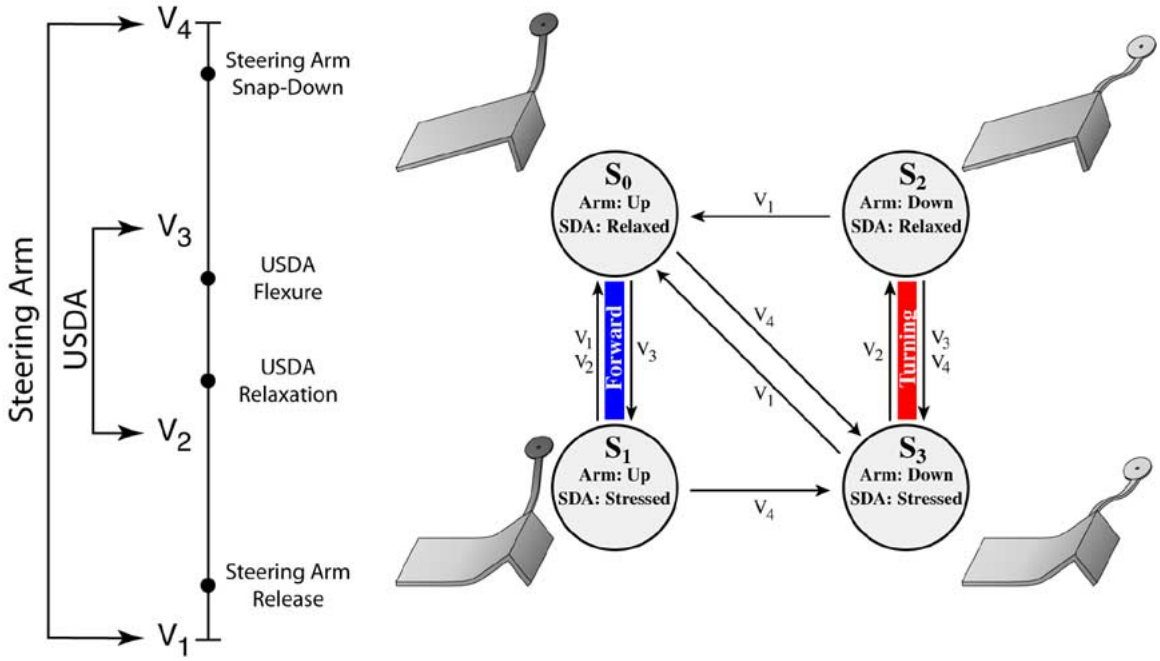

Fig. 2. The state transition diagram of the micro-robot. Four voltages, $V_1 < V_2 < V_3 < V_4$, are used in constructing control waveforms. For the untethered scratch drive actuator (USDA), any voltage below the relaxation voltage will cause it to relax, and any voltage above the flexure voltage will cause it to flex. For the steering arm, any voltage below the release voltage will raise the arm, and any voltage above the snap-down voltage will lower it. The four system states (S_0, S_1, S_2, S_3) correspond to the possible combinations of the states of the steering arm and the USDA. When the voltage is changed, the system will transition to a new state. Since the control voltages of the USDA *nest* within the control voltages of the steering arm, there is a sequence of voltages that allows the system to transition between any pair of states. The device moves forward by repeatedly transitioning between states S_0 and S_1, and turns by transitioning between states S_2 and S_3.

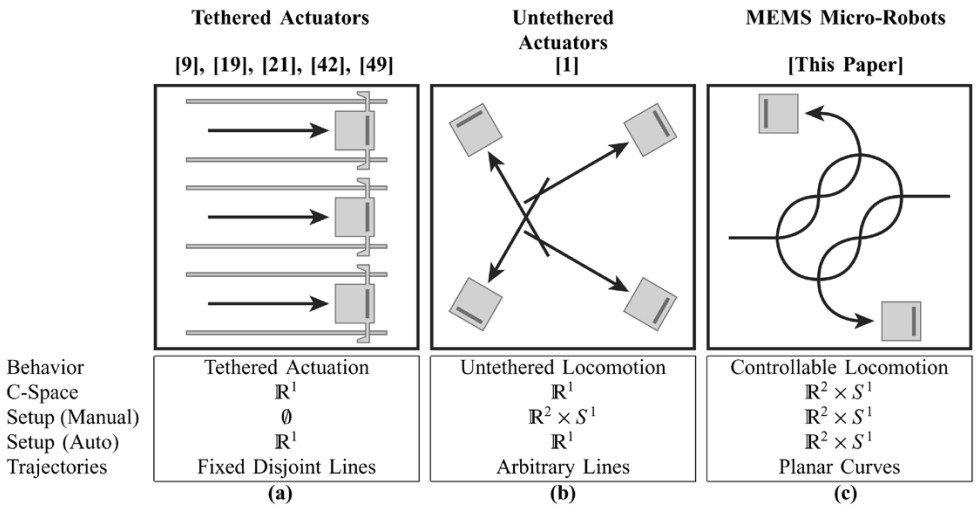

Fig. 3. Progress toward globally controllable MEMS micro-robots. *C-space* (configuration space [22]) reports the total degrees of freedom (DOF) of the device motion. *Setup* reports the DOF possible through initialization of the device's pose (position and orientation) prior to motion either manually with a pair of microprobes (*Manual*), or in an automated fashion (*Auto*). Three classes of device are shown. Panel (a) characterizes the behavior of tethered scratch drive actuators (SDAs). The paths of these devices are constrained to fixed lines [19], [21], [42], [49] or circles [9], [19] that map onto $\mathbb{R}^1$ in configuration space. Panel (b) describes the untethered actuators presented in [1]. These devices also operate in the configuration space $\mathbb{R}^1$, but can be manually initialized in the space $\mathbb{R}^2 \times S^1$, where $\mathbb{R}^2$ is the Euclidean plane of the substrate, and S^1 is the group of 2-D rotations, corresponding to the device's orientation. Hence these untethered devices can move along arbitrary lines in the plane. Panel (c) characterizes the behavior of the micro-robots presented in the current paper. These devices are capable of accessing all points in the configuration space $\mathbb{R}^2 \times S^1$.

motion of micro-robots on planar surfaces. This builds on the untethered locomotion capabilities presented in [1], which in turn generalized the tethered scratch drive actuators described in [19]–[21]. The progression of functional capability can be described formally through the use of configuration space [22]. The configuration space of a rigid body is the set of all possible poses of that body within its workspace. A system is said to be *globally controllable* [23] if every point in the configuration space is reachable from every other point, using the available motions (in this case, translation and turning). These two operations are sufficient to provide our device with global controllability. While the linear untethered scratch drive actuators presented in [1] provide some building blocks for our current power delivery system, the devices in [1] could only be driven in

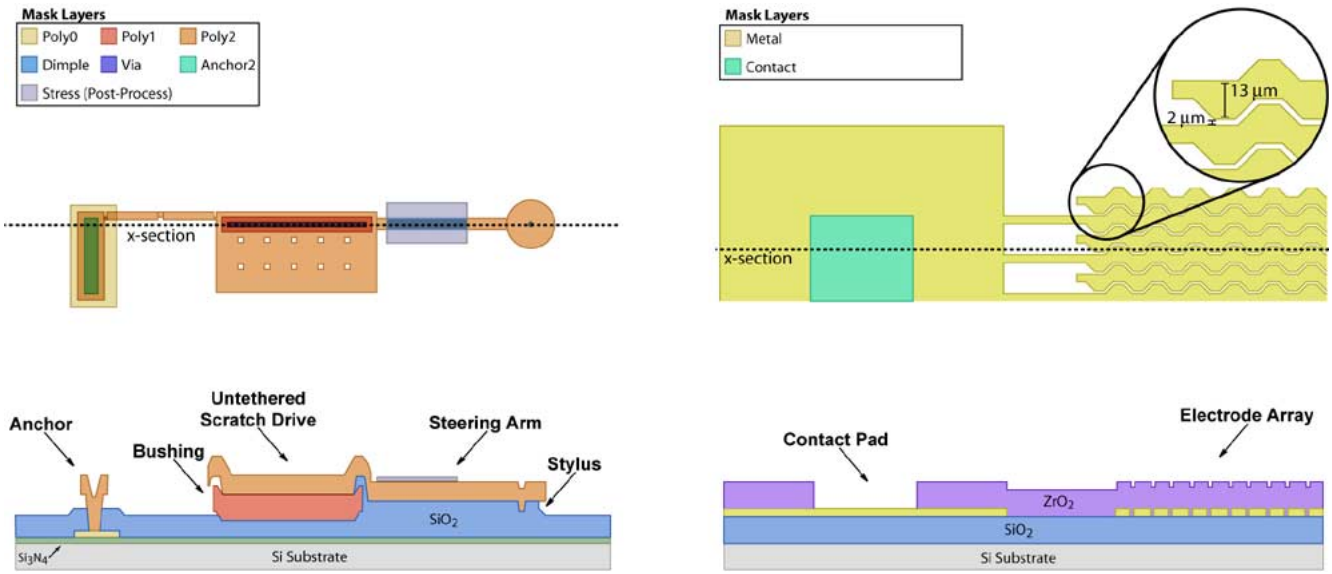

Fig. 4. Fabrication of electrostatic micro-robots. Left: Layout and cross-section of an electrostatic micro-robot just prior to sacrificial release. The device utilizes the first and second released polysilicon layers from the PolyMUMPS process [16], plus an additional layer added during postprocessing. This layer consists of 830 Å of chromium with a tensile residual stress of approximately 550 MPa, and is lithographically patterned with the "Stress" mask (gray, above). After release, the stress in this layer curls the steering arm out of plane. Right: Layout and cross-section of the electrical grids used as the micro-robots' operating environments. The first mask layer defines the metal electrodes, while the second layer defines contact holes through the electrode insulation. The metal electrodes are sandwiched between a layer of thermal silica, and a deposited layer of zirconium dioxide.

straight lines. This paper describes the design, fabrication, and control challenges in making *untethered steerable micro-robots* that can execute complex paths and are globally controllable. These capabilities are essential for micro-robotic applications.

The introduction of a micro-robotic device with side lengths less than 250 μm could extend and enable the set of micro-robot applications that have been previously identified. These include security and surveillance [6], [7]; exploration of hazardous environments [7]; and biomedical research [7], [24]. Of particular interest are those applications which allow a controlled environment for micro-robot operation, in which cleanliness and surface smoothness can be carefully maintained, and in which an ambient power source can be conveniently applied. Such applications include the manipulation and assembly of hybrid microsystems [6], [24]–[28]; micro-scale self-reconfiguring robotics [29]–[34]; and MEMS infosecurity self-assembly [35], where autonomous locomotion of micro-devices is a primary requirement. We envision that the devices, designs, and control systems presented in this paper will enable these applications for micro-robots.

The remainder of this paper will proceed as follows. Section II describes the fabrication of a novel electrostatic MEMS micro-robot. Section III briefly reviews the device's capacitively coupled power delivery mechanism, and extends the mechanism in [1] to incorporate high-κ dielectrics. Sections IV and V discuss the locomotion, steering, communication, and control systems, and Section VI presents measurements of the performance and reliability of these devices in executing a series of micro-robotic tasks.

II. Fabrication

We have fabricated five micro-robots of identical design. All five operated correctly, as will be discussed in Section VI (i.e., the yield was 5 out of 5). The first steps in fabricating the devices were performed through the PolyMUMPS process [16]. This multiuser surface micromachining process consists of three layers of polycrystalline silicon, separated by two sacrificial layers of phosphosilicate glass. The untethered scratch drive actuators and steering arms are both formed from the top layer of polysilicon, as shown in Fig. 4. The bushing is formed by combining the conformalities that result from the PolyMUMPS Dimple Etch and Via Etch, and is approximately 1.5 μm high. Similarly, the stylus at the end of the steering arm is formed from the Dimple Etch conformality, and is 0.75 μm high. After the PolyMUMPS process is complete, we coat the devices with a patterned layer of evaporated chromium. The tensile residual stress in the chromium curves the steering arms upwards. This curvature allows the arm to remain suspended above the substrate, even when sufficient voltage is applied to actuate the scratch drive. Independent control of these two mechanisms will be discussed in detail in Section V.

The electrical grids used as operating environments for the devices were fabricated entirely in-house, and consist of an array of metal interdigitated electrodes on a silicon substrate. The electrodes are insulated from the substrate by a 3–μm-thick layer of thermal silica, and are coated with 0.5 μm of zirconium dioxide, followed by a 300-Å passivation layer of evaporated silica. This dielectric layer allows power delivery to devices placed on top of the electrical grids by capacitive coupling with the underlying electrodes. Fabrication of these electrical grids is illustrated in Fig. 4. Once fabrication is complete, the devices are transferred onto the grids with a vacuum microprobe.

A. Device Fabrication

Fig. 4 shows the layout of one of the devices. The scratch drive plate is 1.5 μm thick, and is defined by a 120 μm by

60 μm rectangle on the third polysilicon layer (Poly2) of the PolyMUMPS process. The scratch drive bushing is composed of a Dimple Etch conformality beneath a sheet of Poly1 that is anchored to the Poly2 layer with the Poly1-Poly2-Via etch. The dimple etch and the via etch each contribute approximately 0.75 μm to the bushing height, resulting in a bushing that is approximately 1.5 μm high. This bushing design has been previously described in [1]. The steering arm is 133 μm long, 8 μm wide, and has an 18-μm-radius disk at its tip. A stylus is defined in the center of this disk by a 1.5-μm-radius dimple that protrudes 0.75 μm beneath the bottom surface. The base of the steering arm is curled so that the tip of the arm is approximately 7.5 μm higher than the scratch drive plate. Since the PolyMUMPS process does not include a layer with enough stress to create this curvature, a layer of tensile chromium is deposited and patterned in the following postprocessing sequence.

The devices are received from the foundry on 1-cm^2 silicon die. After the protective coating of photoresist is removed, the die are soaked in buffered hydrofluoric acid to under-etch the top polysilicon layer. This produces a reentrant surface profile which enables lift-off of subsequent layers.

After rinsing and drying, the die are coated with 830 Å of chromium by thermal evaporation. As deposited, the chrome has an intrinsic tensile residual stress, which produces the necessary curvature in the steering arms upon sacrificial release. For the five devices described in this paper, the corresponding radii of curvature averaged 1.37 mm, with a standard deviation of 0.05 mm. The chrome is lithographically patterned with the "Stress" layer, shown in Fig. 4, and etched in a perchloric-acid-based chrome etchant to transfer the pattern.

Once the chrome pattern has been defined, the sacrificial release etch is performed by soaking in 49% hydrofluoric acid. In addition to releasing the polysilicon structures, this undercuts the excess chrome and detaches it from the substrate. After rinsing in DI water, the die are dehydrated by soaking in isopropyl alcohol, and are then transferred to an ozone-friendly fluorocarbon solvent (based on 2,3-dihydrodecafluoropentane and isopropanol). Slow removal from this solvent ensures very little spotting or unnecessary stiction.

The devices are initially attached to substrate anchors by notched sacrificial beams. These beams are broken with a tungsten microprobe tip to release the devices, as described in [1, p. 951], prior to transferring them to the power-delivery substrates with a vacuum microprobe.

B. Substrate Fabrication

Fig. 4 shows the layout of one of the electrical grids used as operating environments for the micro-robots. These grids consist of interdigitated metal electrodes microfabricated on oxidized silicon substrates. An insulating coating of zirconium dioxide provides a high-impedance dielectric coupling between the electrodes and the devices. Fabrication of these electrical grids was accomplished with the following process sequence.

The sequence begins with a set of 3-in $\langle 100 \rangle$ n-type (phosphorus-doped) silicon wafers. The wafers are cleaned, and oxidized for 20 h at 1100 °C in oxygen, followed by an additional 14 h of wet oxidation using water vapor in a nitrogen carrier gas. The initial dry oxidation produces a high-quality, high-density thermal silica layer, while the subsequent wet oxidation step adds additional thickness [36].

After cooling, the wafers are patterned with the "Metal" pattern shown in Fig. 4 (right), using a bilayer photodefinable resist suitable for liftoff. Metallization is then conducted by resistive boat evaporation at 10^{-6} torr. Three metal layers are evaporated onto the patterned substrates. The middle layer consists of 500 Å of gold, and serves as the conductive bulk of the electrodes. Above and below this are two layers of chromium, each 50 Å thick, which serve as adhesion layers between the gold, the oxidized substrate, and the zirconium dioxide which will be subsequently deposited to insulate the electrodes. The 600-Å electrode thickness helps to prevent unwanted interference in the device motion due to surface geometry.

After metallization, each wafer is cleaved into four 1-inch die. These die are sonicated in photoresist stripper at 45 °C, to lift off the resists and unwanted metal, leaving only the interdigitated electrodes and their associated contact pads. To insulate the electrodes, the die are then coated with 5100 Å of zirconium dioxide, deposited by electron beam evaporation from zirconia powder according to the protocol described in [37]. The process used for zirconia deposition is critical to the quality of the dielectric, and to device performance. Since ZrO_2 dissociates during evaporation, it is important to facilitate recombination at the substrate surface. To do so, the substrates are heated to 100 °C, and oxygen gas is introduced into the chamber to a pressure of 10^{-4} torr. Throughout the deposition process, the chamber pressure is maintained to within $\pm 10\%$ by manually adjusting the oxygen flow. When the zirconia deposition is complete, the chamber is pumped back down to 2×10^{-6} torr, and a 300 Å silica layer is then evaporated. We have found empirically that this over-layer of silica improves the walking performance of scratch drive actuators on zirconia-insulated substrates. We hypothesize that this is due to tribological differences between the zirconia and silica layers.

Once the die have been insulated, they are patterned with the "Contact" mask shown in Fig. 4, and etched in a 5:1 buffered hydrofluoric acid solution for 5 minutes. This etches through the zirconia insulation, stopping on the contact pads.

After rinsing and drying, the substrates are ready for use. The devices are transferred to the electrode arrays by vacuum microprobe, and tungsten-tipped microprobes are used to provide power to the interdigitated electrodes. In Section III, we discuss the delivery of electrical power from these insulated arrays of electrodes to untethered MEMS devices.

III. Power Delivery

In [1], we presented a mechanism for delivering power to untethered MEMS actuators, via a capacitive coupling across a thin film of thermal silica. In this mechanism, a silicon substrate is covered with rows of insulated interdigitated electrodes. When a conductive actuator, such as a scratch drive, rests on top of these electrodes, it forms the capacitive circuit shown in Fig. 5 (right). The electrical potential of the actuator depends on the capacitance between the actuator and the high-voltage

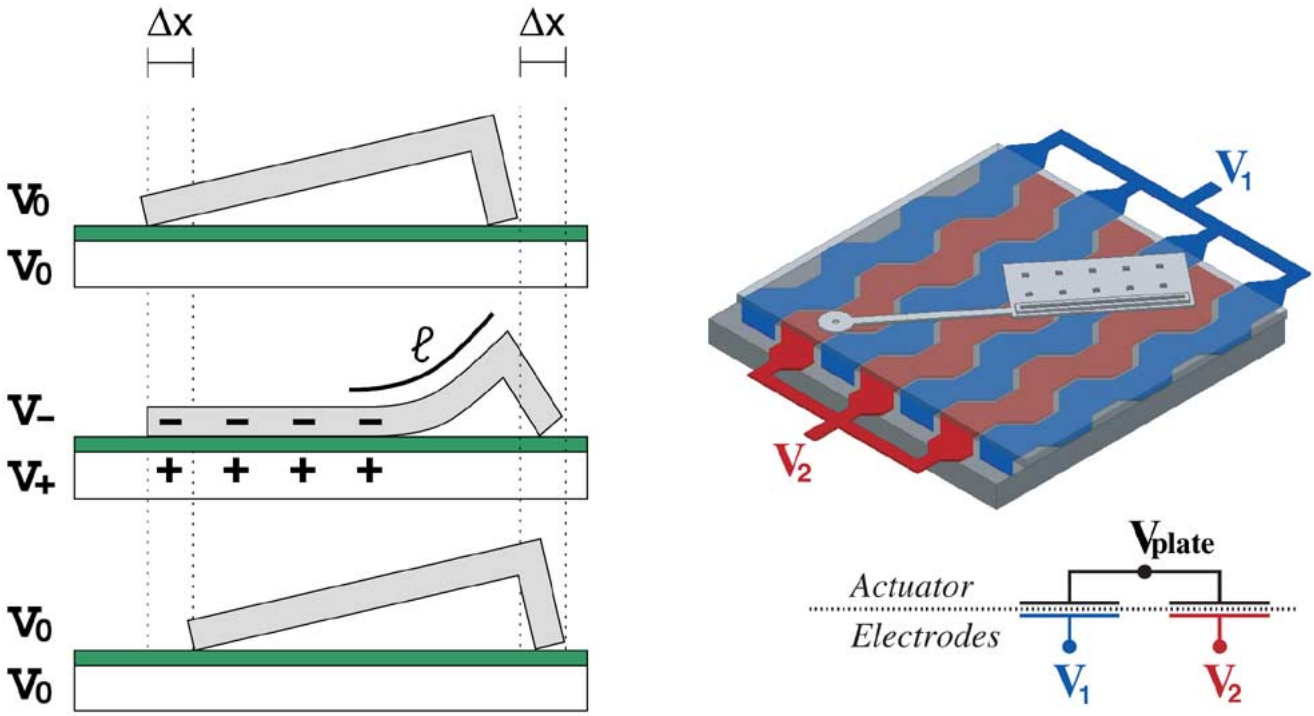

Fig. 5. Left: A schematic of the operation of a tethered scratch drive actuator [19], [21]. The length of the curved region of the plate, ℓ, and the step size, Δx, are determined by the voltage. Right: A schematic of a capacitively coupled power delivery mechanism for untethered actuators [1]. The potential induced on the actuator, $V_{\rm plate}$, is approximately the mean of V_1 and V_2.

electrodes, as compared to the capacitance between the actuator and the low-voltage electrodes. If these two capacitances are roughly equal, and do not change markedly with variation in the position and orientation of the actuator, then the potential of the actuator will be approximately the mean of the electrode potentials. In this way, the actuator can receive a consistent power signal in any position and orientation relative to the underlying electrodes. No position-restricting wires or tethers are required, and the actuator can be operated open-loop.

Once a voltage has been applied between a scratch drive actuator and the electrodes as described above, the actuator will deform as shown in Fig. 5 [19], [20]. Hayakawa *et al.* [38] have calculated the length of the curved region of the scratch drive, ℓ, as follows:

$$\ell = \left(\frac{3Et^3h^2d}{4\kappa\epsilon_0 V^2}\right)^{1/4} \tag{1}$$

where κ is the dielectric constant of the insulator, ϵ_0 the permittivity of free space, h the bushing height, V the applied voltage, E the Young's modulus of the plate material, d the insulator thickness, and t the thickness of the actuator plate. When the voltage is decreased, the flexure in the scratch drive plate relaxes, as shown in Fig. 5. Each time the voltage is cycled, the scratch drive moves forward by a small increment, known as the *step size*. The frequency at which this cycle occurs is known as the *stepping frequency*, and the speed of the actuator is the product of its stepping frequency and its average step size.

Equation (1) shows that there is a trade-off between voltage, insulator thickness, and the relative permittivity of the dielectric. Hence, to improve device performance at a given voltage, we would like an insulator with a high value of κE_{br}, where E_{br} is the dielectric strength. Electrode insulation made from such a material could have a small electrical thickness, (d/κ), allowing the scratch drive to operate at lower voltage for any given plate deflection. For this reason, the high-κ dielectrics under investigation by the semiconductor industry [39] should also be good materials to use as the insulating layer in contact-mode electrostatic MEMS. One such material that performs well in this regard is e-beam-evaporated zirconium dioxide.

To deliver power to our MEMS micro-robots, we have used zirconia-insulated gold electrodes. The small electrical thickness of the insulating layer allows for low-voltage operation, as discussed in Section IV-A, but it also increases the capacitance of the actuator's bushing and the back edge of its plate. As a result, rectangular electrodes similar to those described in [1] would produce larger variations in the capacitance between the actuator and one set of electrodes whenever the bushing or plate edge crosses an inter-electrode gap. This, in turn, would increase the variation in the actuator potential. To reduce this effect, the electrodes are designed to lie on a hexagonal lattice, as shown in Figs. 1 and 4. This way, the contacting edges of the actuator never completely overlap a gap between the electrodes. A more detailed discussion of the electrode design problem can be found in [40].

Details of the fabrication of these substrates were described in Section II-B. The electrodes are thin enough that the capacitance between adjacent electrodes is negligible, so the largest source of parasitic capacitance is between the electrodes and the underlying silicon substrate. This was sufficiently small for the purposes of the experiments conducted in this paper, and could easily be made much smaller by replacing the silicon substrate

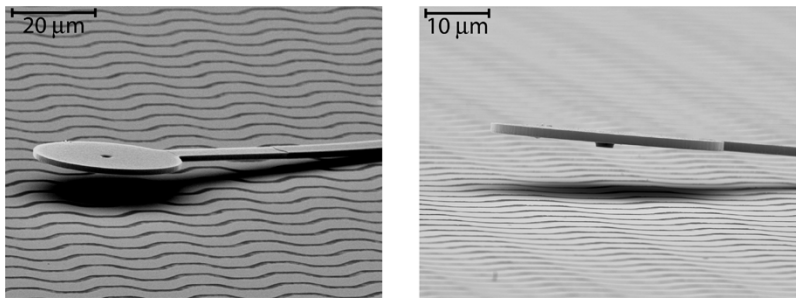

Fig. 6. Electron micrographs of the steering arm subsystem. The stylus used for frictional contact consists of a 0.75-μm dimple, visible beneath the end of the arm. An 18-μm-radius disk increases the electrostatic force on the arm, which is curled upwards to increase the gap between the stylus and the substrate.

with an insulating material such as quartz, or with silicon-on-insulator (SOI) techniques [41]. With these parasitic capacitances removed, the bulk of the delivered power can be focused only on those areas where a device is present.

IV. Steering

The micro-robot controls its direction by raising and lowering its steering arm. Fig. 6 shows a close-up view of this actuator. It consists of a 133-μm-long curved cantilever beam, with a disk at its tip. At the center of the disk, a 0.75-μm-high dimple serves as the stylus for frictional contact. The dimple has a radius of 1.5 μm, and the surrounding disk has a radius of 18 μm.

When the steering arm is in the raised position, the device as a whole behaves like an ordinary untethered scratch drive actuator [1]. In this case, when an oscillating voltage is applied, the device will move forward in a straight line. When the stylus is lowered into contact with the substrate, and the same oscillating voltage is applied, friction at the contact point causes the device to turn.

Steering the micro-robot requires raising and lowering the steering arm while simultaneously operating the scratch drive actuator. When the device is moving forward, the oscillating voltage used to power the scratch drive must not inadvertently pull the stylus into substrate contact. Similarly, when the device is turning, the oscillating voltage used to power the scratch drive must not inadvertently release the stylus from substrate contact. In this section, we derive two waveforms for producing forward and turning motion in the devices. These two signals can be time-sequence multiplexed to produce turning with intermediate radii of curvature, as is shown in Section VI.

A. Actuator Drive Waveform

To produce forward motion, the micro-robot need only actuate its scratch drive actuator. To do so, an ac waveform is applied between adjacent electrodes as shown in Fig. 5. At the peak of this drive signal, the scratch drive flexes into flat contact with the substrate, pushing its front end forward. When the voltage is subsequently decreased, the tail recovers toward the front, creating forward progress. The operation of scratch drive actuators in tethered and untethered systems is described in greater detail in [1], [9], [19], [20], [42].

We would like to choose a waveform for actuating the scratch drive that will not effect the state of the steering arm. Throughout the remainder of the paper, we will call this the *drive waveform*. One critical parameter of the drive waveform is its peak voltage. Linderman [9] and Li [42] have shown correct operation of scratch drive actuators with waveforms having a peak voltage as low as 60 V between the scratch drive plate and an underlying electrode. This corresponds to about 120 V applied between the electrodes of an untethered scratch drive actuator.

Since our devices require the maintenance of a nonzero voltage during the operation of the scratch drive, we must also know how this actuator performs as the baseline voltage of its drive waveform is changed. We tested an untethered scratch drive that was 60 μm long, 120 μm wide, and had a 1.5-μm-high bushing. We operated this untethered scratch drive on one of the zirconia-insulated environments described above, with a 120-ms waveform, consisting of 250 positive 60-μs pulses with a positive dc baseline, followed by 250 negative pulses from a negative dc baseline, with a duty cycle of 25%. We examined the performance of the device as a function of both the peak voltage of the pulses, and the signal baseline. We found that the peak voltage of the pulses applied between adjacent electrodes must be at least 60 ± 10 V to produce motion in the scratch drive, corresponding to approximately 30 ± 5 V between the scratch drive and each electrode. The minimum required peak voltage was consistent for pulses with baseline voltages of 0 V, 20 V, and 40 V. However, when the baseline was raised to 60 V, the device failed to operate with any peak voltage below and including 100 V.

Given the fairly wide range of acceptable drive waveforms, we selected a pulsed wave with peak voltage of 112 V and baseline of 39 V, applied between the electrodes. This corresponds to peak and baseline voltages between the device and the electrodes of approximately 56 and 19 V, respectively. This drive waveform, shown in Fig. 7(a), is adequate to actuate the scratch drive actuator, but does not disturb the steering arm, regardless of whether the arm is in its raised or lowered position. For this reason, the same drive waveform can be applied either when the device is going straight or when it is turning. The behavior of the device is changed only by the position of its stylus. Independent control of the stylus position will be discussed in greater detail in Sections IV-B and V.

Since the voltage on the device must be maintained above zero for considerable lengths of time, it is possible for static charge to accumulate in trap sites within the electrode insulation [43]–[45]. Three characteristics of our chosen drive waveform help to minimize this effect. First, the polarity of the drive

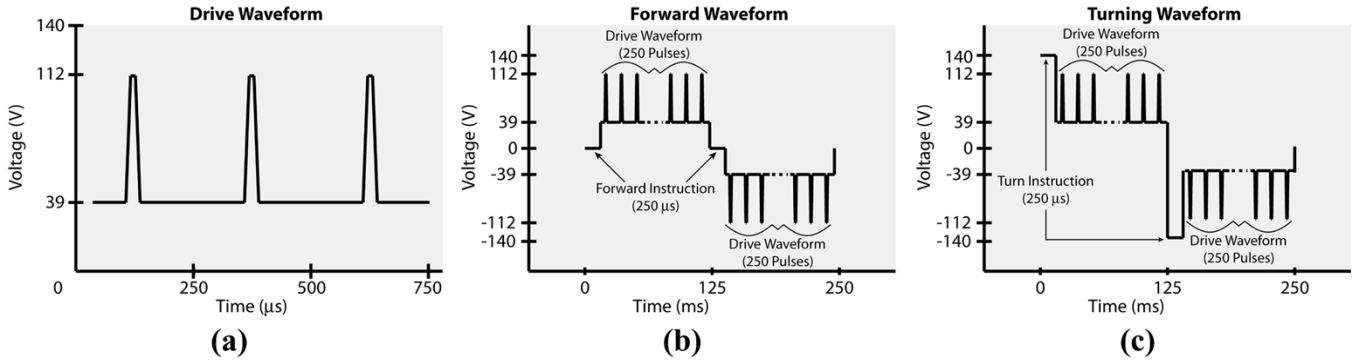

Fig. 7. Control waveforms used for driving the micro-robots at a stepping frequency of 4 kHz. (a) The waveform used to actuate the scratch drive actuator consists of 73-V pulses, with a dc bias of 39 V, applied between adjacent electrodes. These pulses do not disturb the state of the steering arm. (b) The forward waveform lowers the device voltage to zero before initiating the drive waveform, ensuring that the steering arm will be in the raised position. (c) The turning waveform increases the device voltage to 140 V (or -140 V) before initiating the drive waveform, ensuring that the steering arm will be in the lowered position. The polarity of the control waveform is reversed every 250 pulses to limit the effects of parasitic charging. The state of the steering arm is refreshed each time this occurs. In the control waveform segments shown here, the instructions are refreshed at 0 and 125 ms, when the polarity of the control waveform is reversed.

waveform is reversed every 250 pulses. Second, the duty cycle of the waveform is kept small. In all of our test runs (described in Section VI), the high-voltage pulse of the drive signal is 10 μs wide at its peak, 30 μs wide at its base, and has linear ramps for a full-width-half-max pulse width of 20 μs. Depending on the stepping frequency at which we operate the devices (2, 4, 8, or 16 kHz), this corresponds to a duty cycle of 4%–32%. Third, the peak voltage of the drive signal (112 V) is considerably higher than the 60 V required for operation. Our experience suggests that when the devices are driven with peak voltages close to the minimum required voltage, accumulated static charge will cause the devices to fail after only a few seconds of operation. However, when driven with the higher peak voltage, the devices can operate for hours without failure. This performance is discussed in greater detail in Section VI.

B. Turning

Before the micro-robot can turn, the stylus at the tip of its steering arm must be lowered into contact with the substrate. Then, the drive waveform is applied. The frictional force acting on the stylus as the scratch drive actuates causes the device to turn. If the maximum available force of friction on the stylus exceeds the force applied on it by the scratch drive, then the stylus will not translate, and the device will pivot around it.

There are two considerations that must be taken into account in the design of the steering arm. First, the arm must be stiff enough that the peak voltage of the drive waveform (112 V) does not inadvertently pull it into contact with the substrate. Second, it must be flexible enough that, once in contact, the minimum voltage of the drive waveform (39 V) does not allow it to release from the substrate.

To address these considerations, we examine the snap-down and release voltages of the steering arm. When a conductive MEMS cantilever beam is suspended over an electrode, and a voltage is applied between the two, the cantilever will deform somewhat in response to the resulting electrostatic attraction. The magnitude of this electrostatic force scales inversely with the square of the distance between the beam and the electrode, and the mechanical restoring force scales linearly with the beam's deflection. As the voltage is increased, the beam deflection must therefore reach a point of instability where the stylus will snap down into contact with the electrodes. The voltage at which this occurs is called the *snap-down voltage*. When the voltage is subsequently decreased, the tip of the cantilever will remain in contact with the substrate until another instability is reached, and it snaps upward. This latter instability is known as the *release voltage*.

The snap-down voltage of a cantilever beam is one of the earliest problems studied in the field of MEMS. First presented by Nathanson *et al.* in 1967 [13], the electromechanical analysis of cantilever snap-down has since been refined in numerous papers [14], [15], [46], [47]. For simplicity, we will use Nathanson's model here.

Nathanson used a lumped energy minimization model to calculate the snap-down voltage of a cantilever beam as follows:

$$V_{SD} \approx \sqrt{\frac{8Kg_0^3}{27\epsilon_0 A}} \tag{2}$$

where K is the spring constant of the cantilever beam, g_0 is the zero-voltage gap between the cantilever and the electrode, and A is the total area of the cantilever. A similar analysis can be used to calculate the release voltage

$$V_R \approx \sqrt{\frac{2Kg_1^2\,(g_0 - g_1)}{\epsilon_0 A}} \tag{3}$$

where g_1 is the air gap between the cantilever and the electrode, as defined, for example, by a dimple.

These values are, of course, somewhat approximate, so two-dimensional (2-D) finite element models were used to augment (2) and (3) in the design of our steering arms. However, these equations serve to illustrate the following interesting limitation. As mentioned earlier, we would like the micro-robot's steering arm to have a high snap-down voltage, and a low release voltage. In other words, we would like to be able to increase the ratio of the snap-down voltage to the release voltage. We'll call this the

snap ratio. From the above two equations, the snap ratio can be approximated as follows:

$$R_s = \frac{V_{SD}}{V_R} \approx \sqrt{\frac{4g_0^3}{27g_1^2\,(g_0 - g_1)}}. \tag{4}$$

To the extent of the correctness of this rough approximation, the snap ratio is independent of the beam's spring constant and area, but depends strongly on the gaps g_0 and g_1. This suggests that the design parameters most useful for allowing independent control of the scratch drive actuator and the steering arm are *z-axis parameters*.

Due to the largely planar nature of current microfabrication techniques, it can be difficult to parameterize z-axis geometries such as a cantilever's zero-voltage gap, without introducing a new processing step (e.g., a new material layer or etch mask) for each desired parameter value. One way to enable this is to deform parts out-of-plane using stress gradients of bilayer materials. Tsai *et al.* presented a general technique for controlling part curvature, using a top layer of silicon nitride with tensile residual stress [17], [18]. We have adapted this approach for use with a chromium stress layer as described in Section II.

By curving the steering arm out-of-plane, we can increase the snap-down voltage well above the peak voltage of the scratch drive actuator's drive waveform, while keeping its release voltage well below the minimum of the drive waveform. The steering arms on the micro-robots presented in this paper are curved so that their tips are raised approximately 7.5 μm above their base heights. This gives them a snap-down voltage of approximately 60 V, and a release voltage of approximately 15 V. This corresponds to approximately 120 and 30 V, respectively, applied between the electrodes.

Since the drive waveform discussed in Section IV-A nests within the snap-down and release voltages on the steering arm, the stylus can be raised and lowered at will, independent of forward motion. This leads to the instruction set that will be described in Section V.

V. Control

This section describes the instruction set of the MEMS micro-robots, and shows how to encode it in a control waveform to specify device behavior. The devices presented in this paper can, at any given time, be in one of the four distinct states shown in Fig. 2. The stylus can be either up or down, and the scratch drive can be either flexed or relaxed.

In Section IV-B, we showed how the the stylus could be lowered by exceeding the snap-down voltage (approximately 120 V), or raised by dropping the voltage below the release voltage (approximately 30 V). Similarly, in Section IV-A, we showed that the untethered scratch drive could operate with a drive waveform that has a peak voltage of 112 V, and a minimum voltage of 39 V. To operate the scratch drive independently of the stylus position, the drive waveform must fit within the voltage range defined by the steering arm's snap-down and release voltage. By curving the steering arm as described in Section IV-B, we have been able to achieve this.

We can now define four voltages that comprise the instruction set of the micro-robot. See the table at the bottom of the page.

Since V_2 and V_3 fall between the snap-down and release voltages of the steering arm, application of these two voltages will not change the state of the steering arm, as described above.

With these four instructions, we can then model the system as the finite state machine [48] shown in Fig. 2. Here, the set of discrete dc voltages, $\{V_1, V_2, V_3, V_4\}$ comprises the transitions, and the zero-voltage state, S_0, is the start state. The pair of voltages, (V_2, V_3) comprises the drive waveform discussed in Section IV-A. The blue and red transitions in Fig. 2 correspond to the two motion operations of the device that can occur when the drive waveform is applied.

It is easy to see from this state transition diagram that all four system states can be reached, and to compute the voltage sequence required to achieve each one. This leads directly to the control waveforms shown in Fig. 7(b) and (c). Each of these waveforms begins by selecting the system state associated with the desired motion, and then applies the drive waveform. After 250 steps, the waveform polarity is reversed to minimize charge trapping in the dielectric. The desired state is refreshed, and then the drive waveform is continued.

VI. Performance

We tested the performance of the micro-robots in a variety of ways. First, we examined the reliability of the two motion primitives (forward motion and turning) with 10 test runs of each motion primitive for each of five test devices. Second, we examined the speed of the devices as a function of the scratch drive stepping frequency. Third, we looked at how the radius of curvature can be controlled by time-sequence multiplexing the motion primitives. Fourth, we demonstrated teleoperated control of the devices by piloting them through clockwise and counterclockwise rectangular paths. Last, we demonstrated device endurance by continuous operation in turning mode until accumulated error forced the device off of the operating environment.

This section quantifies results from 271 open-loop test runs of five devices, and presents representative segments of additional paths traversed during teleoperation. In all of these test runs, the devices were run under an optical microscope while recording their motions with a digital video camera. Device headings and positions were later extracted by image analysis with precision of $\pm 2^\circ$ and ± 1.6 μm respectively. The position of the device was defined at the center of the scratch drive plate, and its heading was defined by the orientation of the scratch drive bushing. The humidity was controlled to less than 15% RH

$V_1 = 0$ V	$V_2 = 39$ V	$V_3 = 112$ V	$V_4 = 140$ V
Raises Streeing Arm Relaxes Scratch Drive	Relaxes Scratch Drive	Flexes Scratch Drive	Lowers Steering Arm Flexes Scratch Drive

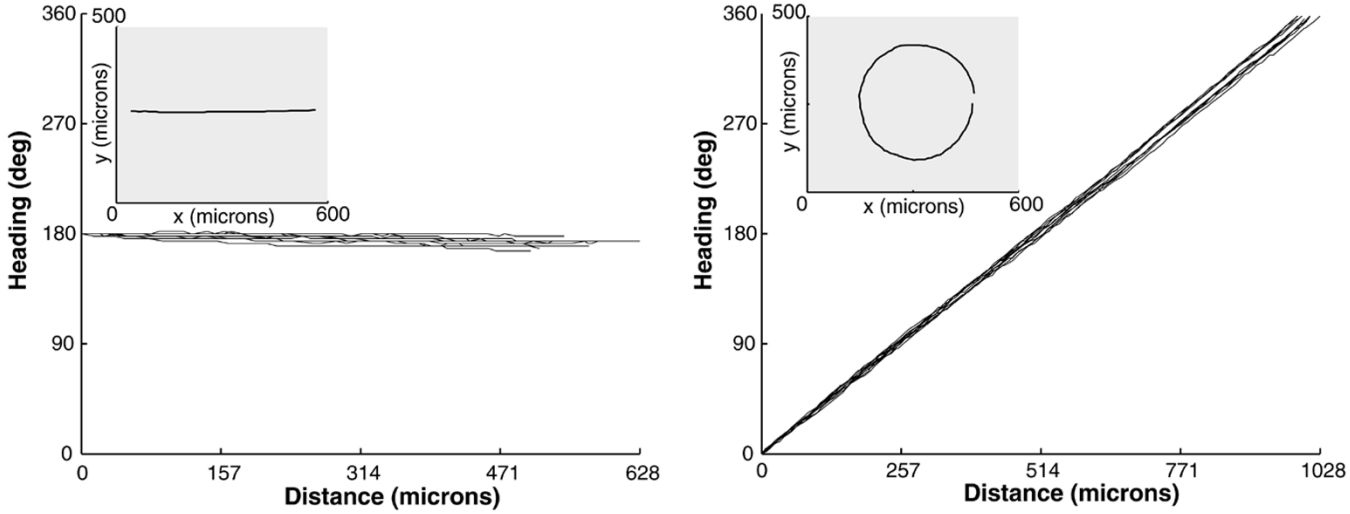

Fig. 8. Open-loop test runs of an electrostatic MEMS micro-robot. Left: The change in device heading over the course of each of 10 trials with the forward waveform at a stepping frequency of 4 kHz. The inset shows a representative path traversed by the device during one of the 10 trials. The average turning rate for these trials was $-14.6°/\mathrm{mm}$. Right: Device heading as a function of distance for each of 10 trials with the turning waveform at a stepping frequency of 4 kHz. The inset shows a representative path. The average turning rate was $353°/\mathrm{mm}$, corresponding to a radius of curvature of 162 μm.

TABLE I
TURNING RATE OF INDIVIDUAL DEVICES

Signal	Open-Loop Turning Rate (std. dev.) [degrees/mm]				
	Device 1	**Device 2**	**Device 3**	**Device 4**	**Device 5**
Forward (4 kHz):	-14.6 (7.8)	9.7 (9.6)	7.8 (14.9)	-21.7 (10.5)	0.4 (13.6)
Turning (2 kHz):	363 (6.0)	341 (7.8)	273 (12.3)	329 (9.2)	305 (5.4)
Turning (4 kHz):	353 (4.9)	338 (4.6)	250 (9.7)	365 (6.5)	321 (8.1)
Turning (8 kHz):	354 (8.3)	367 (4.2)	300 (28.3)	382 (4.8)	360 (6.3)
Turning (16 kHz):	331 (7.0)	373 (3.9)	336 (5.3)	403 (3.3)	379 (3.2)

by a continuous stream of dry nitrogen. Drive waveforms were produced using an Agilent 33 120A arbitrary waveform generator, and amplified with a Trek PZD700-1 high-voltage power amplifier with a gain of 200.

A. Motion Primitives

To test the forward motion, each of five devices was operated with the waveform shown in Fig. 7(b) for 10 10-s trials with a 4-kHz stepping frequency, during each of which the devices travelled an average of 566 μm. For consistency, all of these trials were run approximately parallel to the electrodes. The turning rate of an individual test run is defined by the slope of the best-fit line to the device heading over the course of the test run, plotted as a function of distance travelled. When operated with the forward waveform, the devices should ideally have a turning rate near zero, corresponding to a horizontal line on these plots. Run-to-run deviations in the turning rate of devices operated with the forward waveform should be small relative to the turning rate achievable with the turning waveform (see below). Fig. 8 (left) shows turning rate data for all 10 forward test runs of one device. For all devices combined, the average turning rate over the course of each 10-s forward trial was $-3.7°/\mathrm{mm}$, with a standard deviation of $13.9°/\mathrm{mm}$. Average turning rates for individual devices are shown in Table I, with standard deviations in parentheses. Of course, the errors shown represent open-loop control. With closed-loop control (see Section VI-D), the errors can be corrected by steering (see Section VI-C).

To test the turning motion, the devices were operated with the waveform shown in Fig. 7(c) with a stepping frequency of 4 kHz for 10 trials of one full revolution each. Fig. 8 (right) shows the deviation from initial heading for all test runs of one of these devices. For all devices combined, the average turning rate was $325°/\mathrm{mm}$, which corresponds to a radius of curvature of 176 μm. The standard deviation of the turning rate across all 4 kHz turning runs of all devices was $45.3°/\mathrm{mm}$. Standard deviations for individual devices are considerably lower, and appear in Table I.

B. Device Speed

In addition to the 4 kHz test runs described above, the same five devices were run in turning mode at stepping frequencies of 2, 8, and 16 kHz. There were 10 trials of each device at each frequency. The pulse width of the drive waveform and the period of the control waveforms were unchanged. The different stepping frequencies were achieved by adjusting the duty cycle of the drive waveform.

The average speed of an individual trial is defined as the slope of the best-fit line to the distance travelled, plotted as a function of time. Fig. 9 shows these data for all 10 test runs of one device at a stepping frequency of 4 kHz, and the average speed

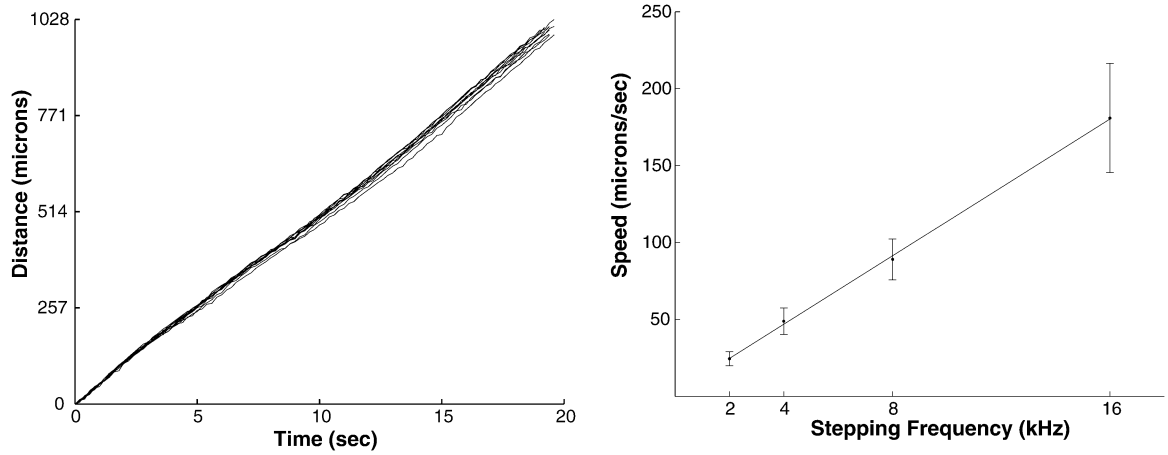

Fig. 9. Left: Path length as a function of time across 10 trials of one device, in response to the turning waveform applied at a stepping frequency of 4 kHz. The average speed across these 10 trials was 51 $\mu\mathrm{m}/\mathrm{sec}$. Right: Speed as a function of changes in the stepping frequency of the turning waveform. Average speed at each frequency was aggregated from 10 test runs of each of five devices. Error bars show one standard deviation above and below the mean.

TABLE II
SPEED OF INDIVIDUAL DEVICES

Signal	Open-Loop Speed (std. dev.) [μm/sec]				
	Device 1	**Device 2**	**Device 3**	**Device 4**	**Device 5**
Forward (4 kHz):	55 (4.4)	58 (2.7)	55 (5.9)	49 (4.0)	66 (2.6)
Turning (2 kHz):	25 (0.3)	28 (0.7)	24 (0.8)	16 (0.4)	29 (0.6)
Turning (4 kHz):	51 (0.8)	53 (0.5)	47 (1.2)	34 (1.0)	59 (0.7)
Turning (8 kHz):	80 (7.6)	93 (1.7)	97 (4.7)	70 (1.1)	105 (2.2)
Turning (16 kHz):	224 (2.9)	147 (1.7)	204 (7.4)	133 (1.3)	197 (6.0)

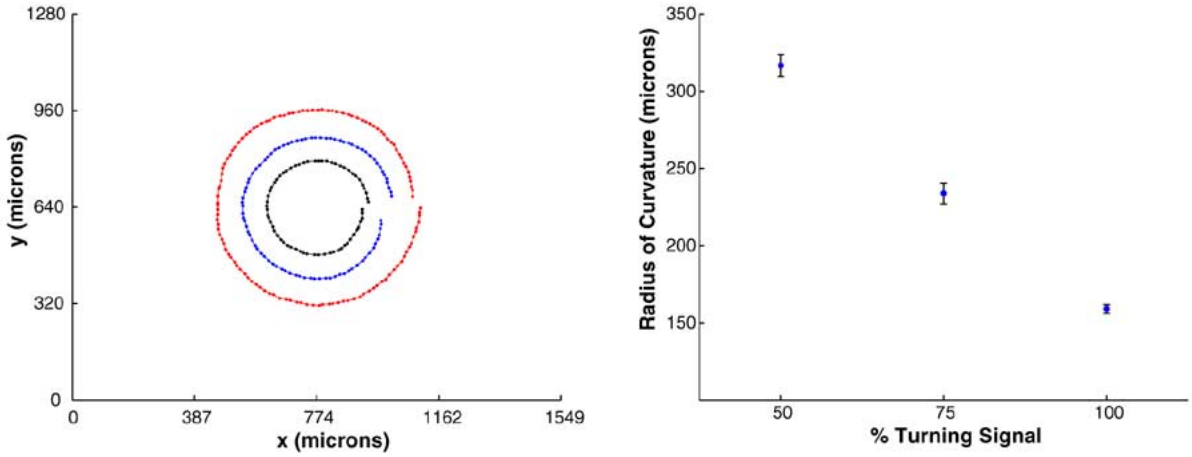

Fig. 10. Path curvature with time-sequence multiplexed control signals. Three control signals were used, each having a stepping frequency of 8 kHz, and a period of 500 ms. Left: Representative paths traversed by a device with waveforms composed of different amounts of turning and forward control signals. In red: 250 ms (50%) turning + 250 ms forward. In blue: 375 ms (75%) turning + 125 ms forward. In black: 500 ms (100%) turning. Right: Radius of curvature as a function of the amount of turning signal, extracted from a series of 10 test runs executed for each of the three different waveforms described above. Error bars show one standard deviation above and below the mean.

across all trials of all devices as a function of stepping frequency. Table II shows average speeds and standard deviations for individual devices at each stepping frequency.

C. Interpolated Steering

The forward and turning behaviors can be combined to produce turning radii with intermediate values. To demonstrate this, we drove a device with a 0.5-second master-waveform composed of turning waveforms interleaved with forward waveforms at a stepping frequency of 8 kHz. We tested waveforms with ratios of 50% turning and 75% turning, and compared these to the results of the test runs with 100% turning described above. There were 10 full-revolution test runs at each of these turning ratios. Fig. 10 shows sample paths from tests runs executed at 50%, 75%, and 100% turning ratio, along with a plot of curvature versus turning ratio averaged across all trials.

D. Teleoperation

With a human operator observing the device behavior, and controlling the waveforms sent to the device, it is possible to

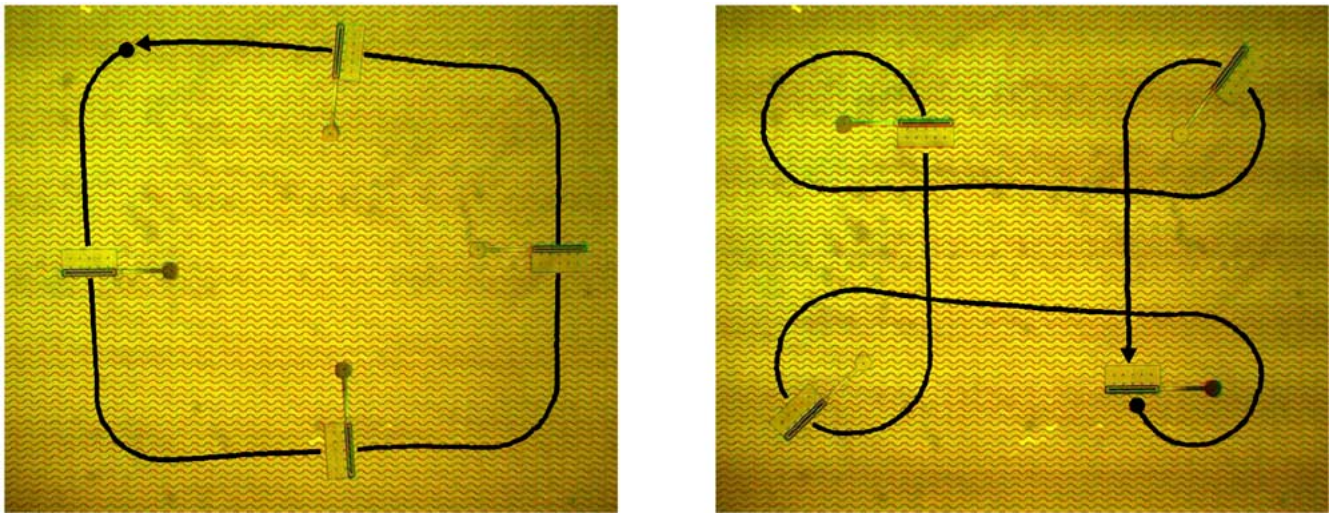

Fig. 11. Sample paths traversed by one of the micro-robots under teleoperated control. The paths traversed by the device were extracted from digital video, and the resulting motion traces are shown in black. Superimposed frames from the video show the position of the device at four different times during each test. Left: Traversal of a counterclockwise rectangular path by turning corners at minimum turning radius. Right: Clockwise paths were achieved by looping at the corners. The videos from which these trajectories were extracted are available on-line here [50].

direct the devices through teleoperation. Of course, it is easier to traverse paths that turn in the direction of the device's steering arm. However, paths that turn in the opposite direction can be followed by looping at corners. Fig. 11 shows clockwise and counterclockwise rectangular paths traversed by one of these devices under teleoperated control.

E. Endurance Testing

To test the reliability of the devices during prolonged operation, we operated one device until the point of failure. The device was piloted to the center of the operating environment, and the turning waveform was applied at a stepping frequency of 4 kHz. Over the course of the next seventy-five minutes, the device executed 215 full rotations, open-loop, without operator intervention, for a total distance travelled of over 35 centimeters. The device eventually stopped when accumulated position error forced it off of the 2.5-mm-wide operating environment. When the device was pushed back onto the operating environment with a microprobe, it continued to operate correctly.

VII. Control System Extensibility

We would like to be able to extend the behavioral complexity of these devices, to produce, for example, devices capable of turning in both directions, or of cooperating in pairs on a common electrical grid. Doing so would require independent control of three or more actuators. To generalize the control system in Section VI, we must be able to store more than two bits of on-board state information. In this section, we will show how to control devices with multiple electrically connected actuators, and will define the design requirements that must be met by those devices if all actuators are to be independently controlled.

Consider a class of n-component electromechanical devices, in which each component can have one of two possible states. We will call these states 0 and 1. States of the system as a whole can then be identified with n-bit binary numbers.

Let $C = \{c_1, \ldots, c_n\}$ be an n-component system where each component, $c_i \in C$, has a binary state and two unique control voltages: $D(c_i)$ and $R(c_i)$. Let this system perform as follows. If the voltage on the system is raised above $D(c_i)$, the component c_i will switch to state 1. If the voltage on the system is lowered below $R(c_i)$, the component will switch to state 0. If the voltage on the system is set to any value between $D(c_i)$ and $R(c_i)$, then the state of the component will maintain whatever value it held before the new voltage was applied. $D(c_i)$, for example, could be the snap-down voltage of a cantilever beam, while $R(c_i)$ could be the release voltage. The voltage range between $D(c_i)$ and $R(c_i)$ denotes the *hysteresis band* of the ith component.

Under what conditions are we able to select *any* arbitrary system state by applying some sequence of voltages? It is necessary and sufficient that the hysteresis bands of all components be *nested*. That is to say, for any two components c_i and c_j, if $R(c_i) < R(c_j)$, then $D(c_j) < D(c_i)$. If this condition holds, then it is simple to select any desired system state. To do so, begin by setting the state of the outermost component in the nesting (i.e., the component with the largest value of $D(c_i)$), and then progress inward.

To demonstrate this control strategy in a more complex system, we built an electromechanical finite state machine (FSM) that consists of three independently controllable cantilevers that together define eight different possible states. The cantilevers are all electrically connected to one another, as would be the case if they were mounted on an untethered micro-robotic system. We used this finite state machine as a test bed for the generalized control system presented above. An electron micrograph of the FSM is shown in Fig. 12.

The cantilevers were fabricated on the Poly2 layer of the PolyMUMPS process [16], and were curved using the postprocessing technique described in Section II. A 0.75-μm dimple at the tip prevents each cantilever from adhering to the substrate after snap-down.

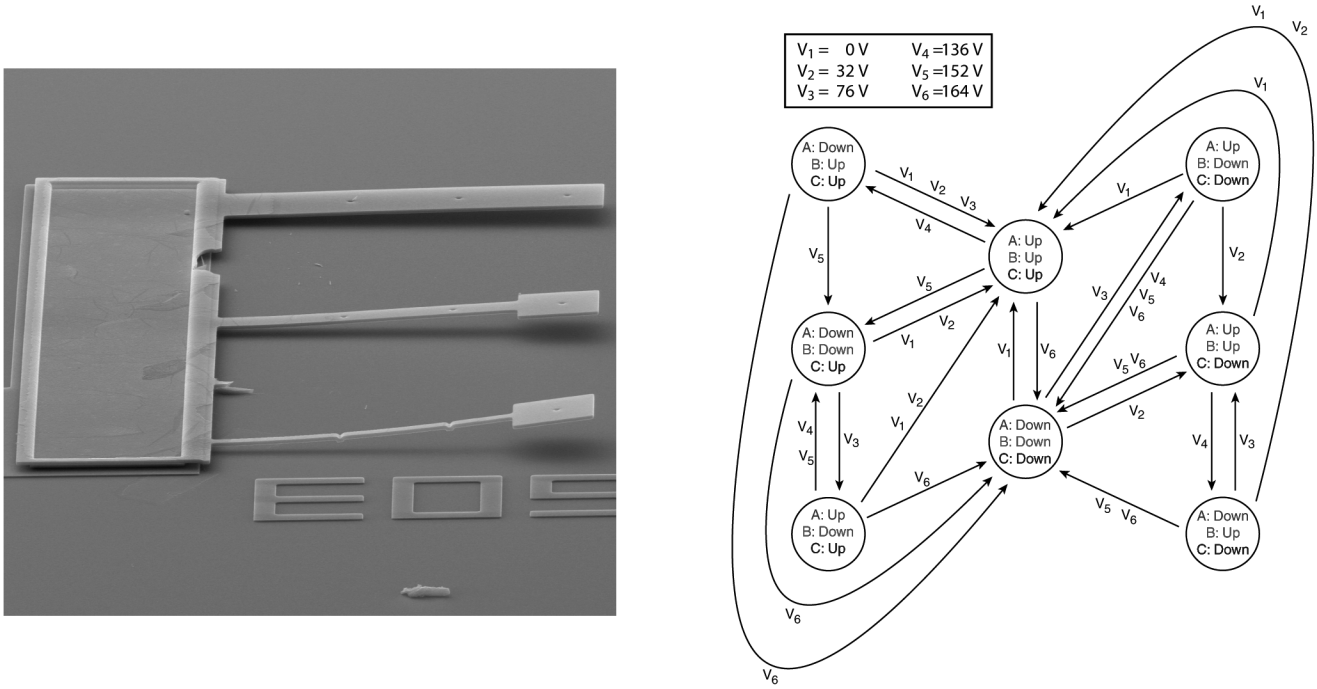

Fig. 12. An eight-state electromechanical finite-state machine (FSM). Left: The FSM consists of three cantilever beams with parameterized width and curvature, as shown in this electron micrograph. All three cantilevers are electrically connected, and must all have the same voltage at any given time. Right The state transition diagram of the FSM. The control voltages (inset, upper left) are chosen from the snap-down and release voltages of each of the individual cantilevers. Since these three voltage pairs nest within one another, there is a sequence of voltages that will cause the system to transition between any two states.

The state of each cantilever is assigned the value 1 if the cantilever is in contact with the substrate, and 0 if the cantilever is not in contact. The state of the FSM as a whole can then be described as a binary number ranging from 000 to 111.

As discussed above, the hysteresis bands of these cantilevers must nest within one another if we are to be able to access all eight states of the system. The curvature of the cantilevers makes this condition possible, as discussed in Section IV-B. The hysteresis loops of the cantilevers were measured with an interferometric microscope, while applying a 5-Hz square-wave signal with no dc bias. The rise time of the signal was sufficiently faster than the response time of the cantilevers that no oscillation was observed. This low-frequency signal helped to reduce the effects of charge trapping in the substrate insulation during the time required to measure the cantilever deflections. The snap-down voltages of these beams were found to be approximately 120, 140, and 160 V, with release voltages of approximately 90, 40, and 10 V, respectively.

Based on these values, we selected a set of six voltages to control the finite state machine: $\{ 0, 32, 76, 136, 152, 164 \}$ (all units in volts). These voltages were selected to be far enough away from the cantilever snap-down and release voltages that variations due to stiction or static charging would not effect the state transitions. Using the eight system states and these six input voltages, we can then construct the state transition diagram shown in Fig. 12.

To demonstrate the correct operation of this finite state machine, we traversed the shortest paths from the start state (000) to each of the other seven states. After each transition, the system state was measured using an interferometric microscope. These seven paths were repeated three times in sequence, without deviation from the system states predicted by the state transition diagram.

VIII. Conclusion

This paper presented an electrostatic MEMS micro-robot that is 1 to 2 orders of magnitude smaller in length than previous micro-robotic systems. This device was shown to perform in a robust and repeatable manner, and could be controlled through teleoperation to traverse complex paths.

The devices are powered through a capacitive coupling with an interdigitated electrode array, so that the devices need not be restricted by the wires and rails that power most electrostatic MEMS devices. Careful design of the mechanical structure of the micro-robot body allows the power signal to double as the control signal. The control information received from this signal is stored as electro-mechanical state information on-board the robot, so that the device can exhibit different behaviors in response to the same drive waveform, based on a previously encoded state.

The communication and control system utilized in these micro-robots exploits electromechanical hysteresis to store state information within the micro-robot body, and is analogous to a four-state finite state machine. This control system was shown to be extensible to more complex systems. Given the extensibility of the control system, a natural next step is to increase the behavioral complexity of the micro-robots themselves. Useful extensions could include the ability to turn in both directions, to move in "reverse," or to manipulate other objects in the environment [1]. One particularly interesting extension would be the parallel operation of multiple micro-robots for cooperative tasks.

ACKNOWLEDGMENT

The authors thank U. Gibson for the use of equipment in her lab, and for many helpful discussions. They also thank D. Balkcom, K. Böhringer, J. Gomez, and S. Prabhakaran for their advice and suggestions. The electron micrographs were taken at the Rippel Electron Microscopy Laboratory, with the help of C. Daghlian. The vacuum microprobe used for device transport was developed with the help of R. Rohl and the National Science Foundation's Research Experience for Undergraduates program.

REFERENCES

[1] B. R. Donald, C. G. Levey, C. D. McGray, D. Rus, and M. Sinclair, "Power delivery and locomotion of untethered micro-actuators," *J. Microelectromech. Syst.*, vol. 12, no. 6, pp. 947–959, Dec. 2003.

[2] S. Baglio, S. Castorina, L. Fortuna, and N. Savalli, "Development of autonomous, mobile micro-electro-mechanical devices," in *IEEE Proc. Int. Symp. Circuits and Systems*, vol. IV, 2002, pp. 285–288.

[3] ——, "Technologies and architectures for autonomous "MEMS" microrobots," in *IEEE Proc. Int. Symp. Circuits and Systems*, vol. II, 2002, pp. 584–587.

[4] P. Basset, A. Kaiser, P. Bigotte, D. Collard, and L. Buchaillot, "A large stepwise motion electrostatic actuator for a wireless microrobot," in *Proc. IEEE Int. Conf. Micro Electro Mechanical Systems*, 2002, pp. 606–609.

[5] T. Ebefors, J. U. Mattsson, E. Kälvesten, and G. Stemme, "A walking silicon micro-robot," *Transducers*, pp. 1202–1205, Jun. 1999.

[6] P. E. Kladitis and V. M. Bright, "Prototype microrobots for micro-positioning and micro-unmanned vehicles," *Sens. Actuators A, Phys.*, vol. A80, no. 2, pp. 132–137, Mar. 2000.

[7] M. H. Mohebbi, M. L. Terry, K. F. Böhringer, G. T. A. Kovacs, and J. W. Suh, "Omnidirectional walking microrobot realized by thermal microactuator arrays," in *Proc. ASME. Int. Mechanical Engineering Congress and Exposition*, Nov. 2001, pp. 1–7.

[8] R. Yeh, E. J. J. Kruglick, and K. S. J. Pister, "Surface-micromachined components for articulated microrobots," *J. Microelectromech. Syst.*, vol. 5, pp. 10–17, Mar. 2001.

[9] R. J. Linderman and V. M. Bright, "Optimized scratch drive actuator for tethered nanometer positioning of chip-sized components," *Transducers*, pp. 214–217, Jun. 2000.

[10] K. Suzuki, I. Shimoyama, and H. Miura, "Insect-model based microrobot with elastic hinges," *J. Microelectromech. Syst.*, vol. 3, pp. 4–9, Mar. 1994.

[11] T. Yasuda, I. Shimoyama, and H. Miura, "Microrobot actuated by a vibration energy field," *Sens. Actuators A*, vol. 43, pp. 366–370, 1994.

[12] H. Miura, T. Yasuda, Y. K. Fujisawa, and I. Shimoyama, "Insect-model based microrobot," *Transducers*, pp. 392–395, Jun. 1995.

[13] H. Nathanson, W. E. Newell, R. A. Wickstrom, and J. R. Davis, "The resonant gate transistor," *IEEE Trans. Electron Devices*, vol. 14, pp. 117–133, Mar. 1978.

[14] P. M. Osterberg and S. D. Senturia, "M-TEST: A test chip for MEMS material property measurement using electrostatically actuated test structures," *J. Microelectromech. Syst.*, vol. 6, pp. 107–118, Jun. 1997.

[15] K. Petersen, "Dynamic micromechanics on silicon: Techniques and devices," *IEEE Trans. Electron Devices*, vol. 25, pp. 1241–1250, Oct. 1978.

[16] K. W. Markus, D. A. Koester, A. Cowen, R. Mahadevan, V. R. Dhuler, D. Roberson, and L. Smith, "MEMS infrastructure: The multi-user MEMS processes (MUMPS)," in *Proc. SPIE—The Int. Soc. Opt. Eng., Micromach., Microfabr. Process Technol.*, vol. 2639, 1995, pp. 54–63.

[17] C.-L. Tsai and A. K. Henning, "Out-of-plane microstructures using stress engineering of thin films," *Proc. Microlithogr. Metrol. Micromach.*, vol. 2639, pp. 124–132, 1995.

[18] C.-L. Tsai, "Three dimensional stress engineered microstructures," Ph.D. dissertation, Thayer School of Eng., Dartmouth College, 1997.

[19] T. Akiyama and K. Shono, "Controlled stepwise motion in polysilicon microstructures," *J. Microelectromech. Syst.*, vol. 2, pp. 106–110, Sep. 1993.

[20] T. Akiyama, D. Collard, and H. Fujita, "A quantitative analysis of scratch drive actuator using buckling motion," in *IEEE Proc. Int. Conf. Micro Electro Mechanical Systems*, Jan. 1995, pp. 310–315.

[21] ——, "Scratch drive actuator with mechanical links for self-assembly of three-dimensional mems," *J. Microelectromech. Syst.*, vol. 6, pp. 10–17, Mar. 1997.

[22] T. Lozano-Perez and M. A. Wesley, "An algorithm for planning collision-free paths among polyhedral obstacles," *Commun. ACM*, vol. 22, no. 10, pp. 560–570, 1979.

[23] H. Hermes, "On local and global controllability," *SIAM J. Contr.*, vol. 12, pp. 252–261, 1974.

[24] P. Dario, R. Valeggi, M. C. Carrozza, M. C. Montesi, and M. Cocco, "Microactuators for microrobots: A critical survey," *J. Micromech. Microeng.*, pp. 141–141, Sep. 1992.

[25] C. Cassier, A. Ferreira, and S. Hirai, "Combination of vision servoing techniques and vr-based simulation for semi-autonomous microassembly workstation," in *Proc. IEEE Int. Conf. Robot. Automation*, May 2002, pp. 1501–1506.

[26] S. Fatikow, J. Seyfried, S. Fahlbusch, A. Buerkle, and F. Schmoeckel, "A flexible microrobot-based microassembly station," in *Proc. IEEE Int. Conf. Emerging Technologies and Factory Automation*, 1999, pp. 397–406.

[27] J. Seyfried, S. Fatikow, S. Fahlbusch, A. Buerkle, and F. Schmoeckel, "Manipulating in the micro world: Mobile micro robots and their applications," in *Proc. 31st Int. Symp. Robotics*, May 1999, pp. 3–9.

[28] H. Worn, F. Schmoeckel, A. Buerkle, J. Samitier, M. Puig-Vidal, S. Johansson, U. Simu, J.-U. Meyer, and M. Biehl, "From decimeter- to centimeter-sized mobile microrobots—The development of the miniman system," *Proc. SPIE Microrobotics and Microassembly III*, vol. 4568, pp. 175–186, 2001.

[29] Z. Butler, R. Fitch, and D. Rus, "Distributed control for unit-compressible robots: Goal-recognition, locomotion, and splitting," *IEEE/ASME Trans. Mechatronics*, vol. 7, pp. 418–418, 2002.

[30] Z. Butler and D. Rus, "Distributed motion planning for 3-d unit-compressible robots," *Int. J. Robot. Res.*, vol. 22, pp. 699–699, Sep. 2003.

[31] K. Kotay and D. Rus, "Locomotion versatility through self-reconfiguration," *Robot. Autonomous Syst.*, vol. 26, pp. 217–217, 1999.

[32] D. Rus, "Self-reconfiguring robots," *IEEE Intell. Transp. Syst.*, vol. 13, pp. 2–2, 1998.

[33] D. Rus and M. Vona, "Crystalline robots: Self-reconfiguration with compressible unit modules," *Autonomous Robots*, vol. 10, pp. 107–107, 2001.

[34] D. Rus, Z. Butler, K. Kotay, and M. Vona, "Self-reconfiguring robots," *Commun. ACM*, vol. 45, pp. 39–39, 2002.

[35] B. R. Donald, "MEMS for Infosecurity," The Office for Domestic Preparedness, Department of Homeland Security, USA, Award Number 2000-DT-CX-K001, 2000–2006.

[36] R. C. Jaeger, *Introduction to Microelectronic Fabrication*, 2nd ed. Englewood Cliffs, NJ: Prentice-Hall, 2002.

[37] J. A. Dobrowolski, P. D. Grant, R. Simpson, and A. J. Waldorf, "Investigation of the evaporation process conditions on the optical constants of zirconia films," *Appl. Opt.*, vol. 28, no. 18, pp. 3997–4005, 1989.

[38] K. Hayakawa, A. Torii, and A. Ueda, "An analysis of the elastic deformation of an electrostatic microactuator," *Trans. Inst. Elect. Eng.Japan*, pt. E, vol. 118-E, no. 3, pp. 205–211, Mar. 1998.

[39] T. P. Ma, "Opportunities and challenges for high-k gate dielectrics," in *2004 IEEE Proc. Int. Symp. Phys. Failure Analysis of Integrated Circuits*, 2004.

[40] C. D. McGray, "Design, fabrication, control, and programming of MEMS micro-robots," Ph.D. dissertation, Comp. Sci. Dept., Dartmouth College, 2005.

[41] S. Wolf, *Silicon Processing for the VLSI Era:—Deep-submicron Process Technology*: Lattice, 2002, vol. 4, pp. 501–570.

[42] L. Li, J. G. Brown, and D. Uttamchandani, "Detailed study of scratch drive actuator characteristics using high-speed imaging," *Proc. SPIE. Reliability, Testing, and Characterization of MEMS/MOEMS*, vol. 4558, pp. 117–123, 2001.

[43] W. M. van Spengen, R. Puers, R. Mertens, and I. D. Wolf, "A comprehensive model to predict the charging and reliability of capacitive RF MEMS switches," *J. Micromech. Microeng.*, vol. 14, pp. 514–521, 2004.

[44] J. Wibbeler, G. Pfeifer, and M. Hietschold, "Parasitic charging of dielectric surfaces in capacitive microelectromechanical systems (MEMS)," *Sens. Actuators, A*, vol. 71, pp. 74–80, 1998.

[45] C. Cabuz, E. I. Cabuz, T. R. Ohnstein, J. Neus, and R. Maboudian, "Factors enhancing the reliability of touch-mode electrostatic actuators," *Sens. Actuators, A*, vol. 179, pp. 245–250, 2000.

[46] P. M. Osterberg, "Electrostatically actuated microelectromechanical test structures for material property measurement," Ph.D., Mass. Inst. Technol., Cambridge, 1995.

[47] S. Pamidighantam, R. Puers, K. Baert, and A. C. Tilmans, "Pull-in voltage analysis of electrostatically actuated beam structures with fixed-fixed and fixed-free end conditions," *J. Micromech. Microeng.*, vol. 12, pp. 458–464, Oct. 2002.
[48] M. Sipser, *Introduction to the Theory of Computation*. Boston, MA: PWS, 1997, pp. 31–47.
[49] P. Langlet, D. Collard, T. Akiyama, and H. Fujita, "A quantitative analysis of scratch drive actuation for integrated x/y motion system," *Transducers*, pp. 773–776, Jun. 1997.
[50] B. Donald, C. Levey, C. McGray, I. Paprotny, and D. Rus. (2005) An untethered, electrostatic, globally-controllable MEMS micro-robot. supplementary videos. Comp. Sci. Dept., Dartmouth College, Tech. Rep. 553. [Online]. Available: www.cs.dartmouth.edu/reports/abstracts/TR2005-553/

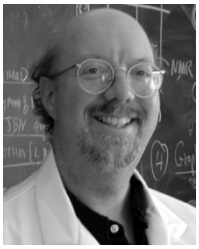

Bruce R. Donald (S'85–M'87) received the B.A. degree from Yale University, New Haven, CT, and the Ph.D. degree from the Massachusetts Institute of Technology (MIT), Cambrdge.

He is the Joan and Edward Foley Professor in the Computer Science Department, Dartmouth College, Hanover, NH, where he holds a joint appointment with the Department of Chemistry and the Department of Biological Sciences. From 1987 to 1998, he was a professor with the Computer Science Department, Cornell University, Ithaca, NY, with a joint appointment in Applied Mathematics.

Dr. Donald has been a National Science Foundation Presidential Young Investigator and a Guggenheim Fellow.

Christopher G. Levey (A'93–M'03) received the B.A. degree in physics from Carleton College, Northfield, MN, in 1977 and the Ph.D. degree in physics from the University of Wisconsin-Madison in 1984.

He was a Member of the Technical Staff at AT&T Bell Labs until 1986, when he joined the faculty of Dartmouth College, Hanover, NH. His research as a faculty member in the Physics Department involved high-temperature superconductor devices. After a sabbatical leave at Bellcore, he joined the Thayer School of Engineering at Dartmouth College in 1993. His research there has included work on a variety of microfabricated devices, including stress-engineered MEMS structures, binary optics, programmable microvapor dispensers, integrated inductors, nanotextured surfaces, and MEMS-based robots. He is the Director of the Microengineering Laboratory at the Thayer School of Engineering at Dartmouth College.

Craig G. McGray (M'03) received the Ph.D. degree in computer science from Dartmouth College, Hanover, NH, in 2005.

He is now a researcher with the National Institute of Standards and Technology. His research interests include microelectromechanical systems, micro-robotics, and metrology systems for micro- and nanotechnologies.

Igor Paprotny received the B.S. degree in mechatronics from NKI College of Engineering, Norway, and the B.S.E. and M.S.E. degrees in industrial engineering from Arizona State University.

He is a Ph.D. student in the Computer Science Department, Dartmouth College, Hanover, NH. He has more than three years of professional experience in the semiconductor industry. His current research interests lie in micro-robotics, focusing on design and implementation of complex micro-robotic systems using microfabrication technologies.

Daniela Rus received the Ph.D. degree in computer science form Cornell University, Ithaca, NY.

She is an Associate Professor with the the Electrical Engineering and Computer Science Department, Massachusetts Institute of Technology (MIT), Cambrdge. Previously, she was a Professor with the Computer Science Department, Dartmouth College, Hanover, NH. Her research interests include distributed robotics, mobile computing, and self-organization.

Dr. Rus was the recipient of an NSF Career award and an Alfred P. Sloan Foundation Fellowship. She is a class of 2002 MacArthur Fellow.